

Article

PyDotSim: a Python-based self-consistent simulation tool for excitonic states in semiconductor quantum dots under electric and magnetic fields

Christian Heyn* 

Center for Hybrid Nanostructures (CHyN), University of Hamburg, Luruper Chaussee 149, 22761 Hamburg, Germany

* Correspondence: heyn@physnet.uni-hamburg.de

Abstract: A Python based three-dimensional (3D) finite element method (FEM) simulation tool for the excitonic states in a semiconductor quantum dot (QD) is described. The underlying model is based on effective mass approximation for the electron and hole single-particle states and includes multi-particle refinements by the Coulomb interaction and by considering correlation effects in a self-assembled fashion. In addition to the energy of the excitonic optical emission, also the radiative lifetime can be simulated. A graphical user interface (GUI) integrates the convenient selection of several QD shapes with varied sizes, the QD and barrier materials, uniform external electric and magnetic fields, and the field of point charges. Simulated probability densities are directly plotted for illustration. In addition to single simulation runs, also series of simulations with varied parameters are possible. Due to the easy GUI-based access, the simulation tools is suggested for education and for experimenters who wants to predict or evaluate their experimental findings. For a demonstration of the model, simulation results are compared to experimental data obtained using micro-photoluminescence from single GaAs cone-shell QDs (CSQDs). These CSQDs have a unique shape which allows a wide tunability of the charge carrier probability densities by external electric and magnetic fields. Studied points include the dependence of the exciton energy and the exciton-biexciton splitting on the QD size, a significant Stark-shift and the transformation of the hole probability density from a dot into a quantum ring in a vertical electric field, a novel strong-weak confinement regime and its influence on the radiative lifetime, the broadening of the exciton peak and a possible origin for blinking induced by point charges, the possibility to store photoexcited charge carriers in combined electric and magnetic fields, and optical Aharonov-Bohm oscillations.

Keywords: Quantum dot, quantum ring, simulation, effective mass approximation, Coulomb interaction, correlation, exciton, electric field, magnetic field, photoluminescence

Citation: . *Nanomaterials* **2023**, *1*, 0.

<https://doi.org/>

Received:

Revised:

Accepted:

Published:

Copyright: © 2024 by the authors. Submitted to *Nanomaterials* for possible open access publication under the terms and conditions of the Creative Commons Attribution (CC BY) license (<https://creativecommons.org/licenses/by/4.0/>).

1. Introduction

Semiconductor quantum dots (QDs) are fascinating objects of the nanoworld and highly interesting for fundamental research as well as for applications. This great relevance was honored by the Nobel Prize in Chemistry 2023. With a size smaller than the De Broglie wavelength for electrons, the energy levels of confined charge carriers are discrete and QDs are often called artificial atoms. QDs are usually fabricated by synthesis [1] or using molecular beam epitaxy (MBE) [2–9]. In particular single MBE grown epitaxial QDs are highly attractive for optical quantum technologies [10–16] due to the almost perfect crystal quality and the precisely controlled optical properties.

Several theoretical approaches are introduced to model the QD quantized energy levels, like the atomistic [17,18] or the $k \cdot p$ theory [19–22]. The present simulation model is more simple and based on the effective mass approximation [23]. Thus, the precision of the model is not high enough for the evaluation of very small effects like the exciton fine-structure splitting [17,20,24–26]. Nevertheless, there are a large number of interesting

effects that are accessible and simulations run on conventional desktop PCs with rather short computation times. The simulation model includes multi-particle refinements by the Coulomb interaction as well as by correlation effects and considers uniform external electric and magnetic fields, and the field of point charges. In addition to the energy of the excitonic emission, also the radiative lifetime can be simulated. The goal is to provide a convenient and fast simulation tool for the QD optical properties which is completely written in the programming language Python 3 using only established standard libraries. The Python code is tested on standard desktop PCs with several Python interpreters and published as open-source at <https://github.com/HappyCodingz/PyDotSim>.

The manuscript is organized as follows. Section 2 describes the mathematics of the model and section 3 the dependence of the accuracy and the computation time on simulation parameters, such as the number of finite element mesh cells. Section 4 discusses examples to demonstrate the possibilities of the simulation tool, where mostly so called cone-shell QDs (CSQDs) are addressed, which allow a wide tunability of the charge-carrier probability densities by external electric and magnetic fields [27–30]. In detail, the exciton energy and the exciton-biexciton splitting as function of the QD size, the vertical electric field induced Stark-shift and the transformation of the hole probability density from a dot into a quantum ring, a novel strong-weak confinement regime and its influence on the radiative lifetime, point charges as origin for the broadening of the exciton peak and for the QD blinking, the storage of photoexcited charge carriers by combined electric and magnetic fields, and optical Aharonov-Bohm oscillations are addressed.

2. Simulation model

The present simulation model is based on the finite element method (FEM) and solves the three dimensional (3D) Schrödinger equation in effective mass approximation to compute the single-particle envelope wave function and eigenvalues. Since optical emission from a QD is caused by radiative recombinations of electrostatically coupled electrons and holes (so-called excitons), both charge carrier types must be computed. To consider also interactions between the charge carriers, the simulated electron and hole wave functions are analyzed and the Coulomb interaction is calculated as well as the influence of correlation effects between charge carriers. The underlying FEM mesh consists of N^3 cubic mesh cells with equal volume w_C^3 . In view of epitaxial wafer-based QD fabrication methods, the Cartesian coordinates x and y are in the plane of the wafer surface and z represents the typical growth direction perpendicular to the wafer surface. The QD center is at $x = y = z = 0$. We note that the wave function barycenters (analogous to a center of mass) can deviate from this position.

2.1. Finite-difference method (FDM)

The 3D Schrödinger equation is $\left(-\frac{\hbar^2}{2m^*}\nabla^2 + V\right)\Psi = H\Psi = E\Psi$, where \hbar is Planck's constant h divided by 2π , m^* is the charge carrier effective mass, V is the potential energy, E is the energy of the quantized state, Ψ is the envelope of the charge carrier wave function, and $H = -\frac{\hbar^2}{2m^*}\nabla^2 + V$ is the Hamiltonian. Following the FEM approach, the potential V is discretized using a cubic mesh with N^3 mesh cells of equal size. Now, the Schrödinger equation is computed for each individual mesh cell. Using the finite-difference method (FDM), the term $\nabla^2\Psi$ is discretized assuming a linear slope between neighbored mesh cells. This approach is described in detail in Ref. [31].

For illustration we discuss now a one-dimensional (1D) model, where FDM considers two neighbors at $i - 1$ and $i + 1$ for a mesh cell with index i and position x . FDM approximates here $\nabla^2\Psi = \frac{\delta^2\Psi(x)}{\delta x^2} = \frac{\Psi_{i-1} - 2\Psi_i + \Psi_{i+1}}{w_C^2}$, with the size w_C of the mesh cell. For the whole

system including $i = 1 \dots N$ this yields N linear equations $-\frac{\hbar^2}{2m^*w_C^2}(\Psi_{i-1} - 2\Psi_i + \Psi_{i+1}) + V_i\Psi_i = E_i\Psi_i$. These equations can be written in a matrix form of the Hamiltonian

$$H = -\frac{\hbar^2}{2m^*w_C^2} \begin{pmatrix} -2 & 1 & 0 & \dots & 0 \\ 1 & -2 & 1 & \dots & 0 \\ 0 & 1 & -2 & \dots & 0 \\ \dots & \dots & \dots & \dots & \dots \\ 0 & 0 & 0 & \dots & -2 \end{pmatrix} + \begin{pmatrix} V_1 \\ V_2 \\ V_3 \\ \dots \\ V_N \end{pmatrix}$$

In a 3D simulation model with N^3 mesh cells, the above equations are expanded and in total six neighbors along x , y , and z must be considered. The Hamiltonian represents a matrix eigenvalue problem, which can be solved in Python using the SciPy library via the function `scipy.sparse.linalg.eigsh()` (<https://docs.scipy.org/doc/scipy/reference/generated/scipy.sparse.linalg.eigsh.html>). Since most elements of the Hamiltonian matrix equal zero, a SciPy compressed (sparse) matrix is used to reduce the memory consumption. The such computed eigenvector yields the wave function Ψ and the eigenvalues yield the energy E of the state.

2.2. Potential V

The potential of an individual mesh cell at a position vector $r(x, y, z)$ is

$$V(r) = V_M + V_F + V_{PC} + V_B + V_C \quad (1)$$

and includes the material related confinement potential V_M , the potential V_F induced by a uniform electric field, the potential V_{PC} of a point charge, the potential V_B given by a magnetic field, and the correlation related potential V_C , which is caused by additional charge carriers inside the dot. Further potentials like a strain-induced piezoelectric field are not considered at this stage.

The QD confining potential is given by the materials and the QD shape, where we define $V_M = 0$ inside the QD and the value inside the barrier reflects the bandgap discontinuity. For instance, an $\text{Al}_{0.34}\text{Ga}_{0.66}\text{As}$ barrier with an embedded GaAs QD has at a temperature of $T = 4$ K a discontinuity of $V_M = 0.293$ eV for electrons and $V_M = 0.172$ eV for holes [32]. Considered QD shapes are an ellipsoid, a disk, a cone, and a cone shell. The cone-shell shape is motivated by our recent experiments on such structures [27–30,33].

The potential induced by a uniform electric field F_x along x -direction is $V_F = q_jxF_x$, where $q_j = q$ for electrons and $q_j = -q$ for holes, and q is the elementary charge. For a field along z -direction, the above x is replaced by z .

The field of a negative point charge located at a position $r_{PC}(x_{PC}, y_{PC}, z_{PC})$ yields a potential $V_{PC} = q_j/(4\pi\epsilon r_{PC})$, with the QD material dielectric constant ϵ .

And finally, a magnetic field B oriented along z -direction yields a potential [28] $V_B = \frac{\hbar^2L^2}{2m^*(x^2+y^2)} + \frac{\hbar q_jBL}{2m^*} + \frac{q_j^2B^2}{8m^*}(x^2+y^2)$, with the angular momentum quantum number L . Here, the simulation of excitons require to distinguish L_e for the electron and L_h for the hole.

Since the simulation field is finite, we have to consider the Dirichlet boundary condition which requires far away from the QD that Ψ equals zero. This is realized by setting the potentials at the outer borders of the simulation field to very large values $V = 100$ eV.

2.3. Self-consistent charge carrier correlation

Operationally, simulations are started by creating the matrix containing the potentials for the electron and hole according to Eqn. 1. Here, initially $V_C = 0$ is assumed. Now, the electron and hole single-particle wave-functions Ψ_e , Ψ_h and the corresponding eigenenergies E_e , E_h are computed by solving the Schrödinger-equation via the Hamiltonian matrix using the FDM method (see section 2.1). For GaAs QDs inside an $\text{Al}_{0.34}\text{Ga}_{0.66}\text{As}$ barrier the electron effective masses are $m_e^* = 0.067m_0$ inside the dot and $m_e^* = 0.086m_0$ inside the

barrier, with the free electron mass m_0 . The hole masses are $m_h^* = 0.51m_0$ and $m_h^* = 0.59m_0$, respectively.

Charge carrier correlation means the deformation of a charge-carrier probability density due to the presence of additional charge carriers inside a QD. If correlation is considered, the electron and hole charge distributions $p_e(r) = q|\Psi_e(r)|^2$ and $p_h(r) = q|\Psi_h(r)|^2$ are calculated from the single-particle wave functions simulated in the first step. This gives the corresponding potentials $V_{C,e}(r)$ and $V_{C,h}(r)$ via Poisson's equation. In a next simulation step, the Schrödinger-equation is solved again to determine the electron and hole wave-functions and the eigenenergies, but now under consideration of the potential V_C induced by the additional charge carriers. For an exciton, the electron is computed considering the potential of the additional hole via $V_C = V_{C,h}$ and the hole via $V_C = V_{C,e}$. In addition to an exciton composed of one electron and one hole, also multi-excitonic states like biexcitons and trions can be simulated. For a biexciton the correlation potential of an electron becomes $V_C = V_{C,e} + 2V_{C,h}$ and for a hole $V_C = 2V_{C,e} + V_{C,h}$. This self-consistent approach for the charge-carrier correlation can be repeated to increase the accuracy, where N_{SC} is the number of self-consistent loops and $N_{SC} = 0$ means no correlation correction.

The outcome after this step are the electron and hole wave-functions Ψ_e , Ψ_h and the corresponding eigenenergies E_e , E_h .

2.4. Wave function analysis

Excitons represent many-particle systems that are composed of negatively charged electrons and positive holes in different configurations. The exciton binding energy summarizes repulsive and attractive Coulomb interactions and can be calculated from the simulated wave functions using the Coulomb integral

$$C_{ij} = \frac{q_i q_j}{4\pi\epsilon r} \iint \frac{|\Psi_i(r_i)|^2 |\Psi_j(r_j)|^2}{|r_i - r_j|} dr_i dr_j \quad (2)$$

with $i, j = e$ for electrons and h for holes, and $q_e = q$ and $q_h = -q$. Now, the exciton energy is given by

$$E_X = E_e + E_h + C_{eh} \quad (3)$$

with the attractive electron-hole Coulomb interaction energy C_{eh} . The biexciton energy is

$$E_{XX} = 2E_e + 2E_h + 4C_{eh} + C_{ee} + C_{hh} \quad (4)$$

with the repulsive electron-electron and hole-hole Coulomb interaction energies C_{ee} and C_{hh} . The biexciton binding energy giving the splitting between the exciton and biexciton energies is the energy gain when two excitons form a biexciton

$$\Delta E_{XX} = 2E_X - E_{XX} = -2C_{eh} - C_{ee} - C_{hh} \quad (5)$$

Exchange interaction [34] and the resulting spin-splitting of the energies is not considered at the present state of the simulation model.

To evaluate the energy of optical recombinations and compare simulation results for instance with photoluminescence (PL) experiments, the bandgap energy E_g of the QD material must be added to the exciton energy

$$E_{X,PL} = E_g + E_X \quad (6)$$

For instance, the temperature dependent bandgap of GaAs is described by the well known Varshni equation E_g [eV] = $E_{g0} - c_1 T^2 / (c_2 + T)$, with the parameters $E_{g0} = 1.519$ eV, $c_1 = 0.5405$ meV/K, and $c_2 = 204$ K [32].

The oscillator strength for a homogeneous medium is calculated from the overlap integral $\langle \psi_e | \psi_h \rangle^2$ between the electron and hole envelope wave functions in the QD [35] $f = E_P \langle \psi_e | \psi_h \rangle^2 / E_{X,PL}$, with the Kane energy E_P (for GaAs $E_P = 28.8$ eV). This approach

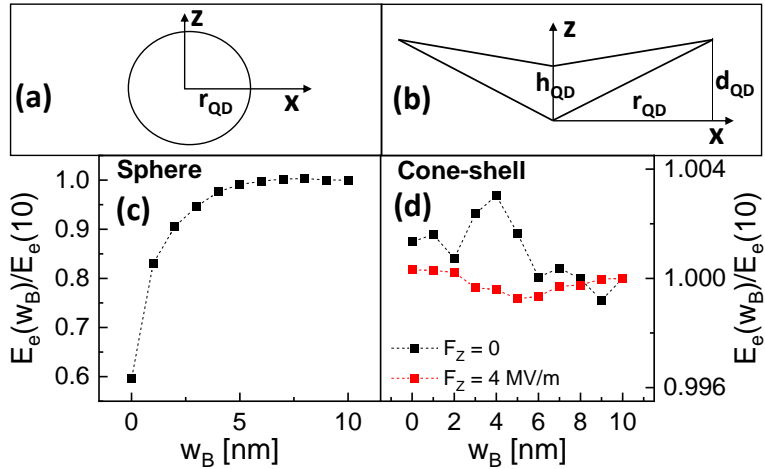


Figure 1. (a) Cross-sectional scheme of a sphere-shaped QD with radius r_{QD} . (b) Cross-sectional scheme of a rotational-symmetric cone-shell QD with indicated structural parameters. (c) Influence of the border width w_B on the relative single-particle energy $E_e(w_B)/E_e(10 \text{ nm})$ of the electron ground-state of a sphere-shaped QD with $r_{QD} = 5 \text{ nm}$ and $w_C = 0.25 \text{ nm}$. (d) Influence of w_B on $E_e(w_B)/E_e(10 \text{ nm})$ of a CSQD with $r_{QD} = 35 \text{ nm}$, $d_{QD} = 19 \text{ nm}$, and $h_{QD} = 13.6 \text{ nm}$. The simulations are done using $w_C = 1 \text{ nm}$ and without or with a vertical electric field F_z .

is related to the so-called strong confinement regime [35,36], where the QD radius r_{QD} is smaller than the bulk exciton Bohr radius $\lambda_B = 4\pi\epsilon\hbar^2/(m_x^*q^2)$, with the exciton effective mass $m_x^* = (1/m_e^* + 1/m_h^*)^{-1}$. For GaAs, $\lambda_B = 11.7 \text{ nm}$. Now, the radiative lifetime of an exciton is calculated from the oscillator strength via

$$\tau_B = 3\hbar^2 c^3 \epsilon_0 m_0 / (2n\pi q^2 E_{X,PL}^2 f) \quad (7)$$

Furthermore, mostly for illustration, also the barycenters of the simulated Ψ_e and Ψ_h can be calculated.

3. Accuracy and computation time

This section addresses the influence of the simulation parameters on the accuracy of the obtained results and on the computation time. The present simulations are done using a standard desktop PC with 16 GB RAM. That means the processor power is limited and the selection of for instance a finer FEM-mesh with a higher number of mesh-cells for a more accurate modeling costs a longer computation time.

3.1. Single-particle accuracy and computation time

The cubic 3D simulation field with total volume $w_F^3 = (Nw_C)^3$ is composed of N^3 cubic mesh cells with respective volume w_C^3 . Due to the limited size of the simulation field, the studied structures are surrounded by a finite border of the barrier material. The width of the border $w_B = w_F/2 - r_{QD}$ is anisotropic, with the QD radius r_{QD} . Here, we define the thinnest border width as w_B . The tests described in this section are done for a GaAs QD in an $\text{Al}_{0.34}\text{Ga}_{0.66}\text{As}$ barrier.

The first step studies the influence of the border width w_B for two examples: a sphere-shaped QD (Fig. 1(a)) with radius $r_{QD} = 5 \text{ nm}$ and a cone-shell QD (CSQD) with $r_{QD} = 35 \text{ nm}$, $d_{QD} = 19 \text{ nm}$, and $h_{QD} = 13.6 \text{ nm}$ (Fig. 1(b)). The CSQD structural parameters are taken from a previous publication [27] as an example of a typical structure. Figure 1c shows the strong influence of w_B on the single-particle energy E_e of the electron ground-state of a sphere. Here, the charge carrier probability density is distributed over the hole QD and is sensitive to the presence of the simulation field boundaries. For $w_B \geq 5 \text{ nm}$ the value of E_e saturates and the deviation $1 - E_e(w_B)/E_e(10 \text{ nm})$ becomes less than 1 %. For a CSQD

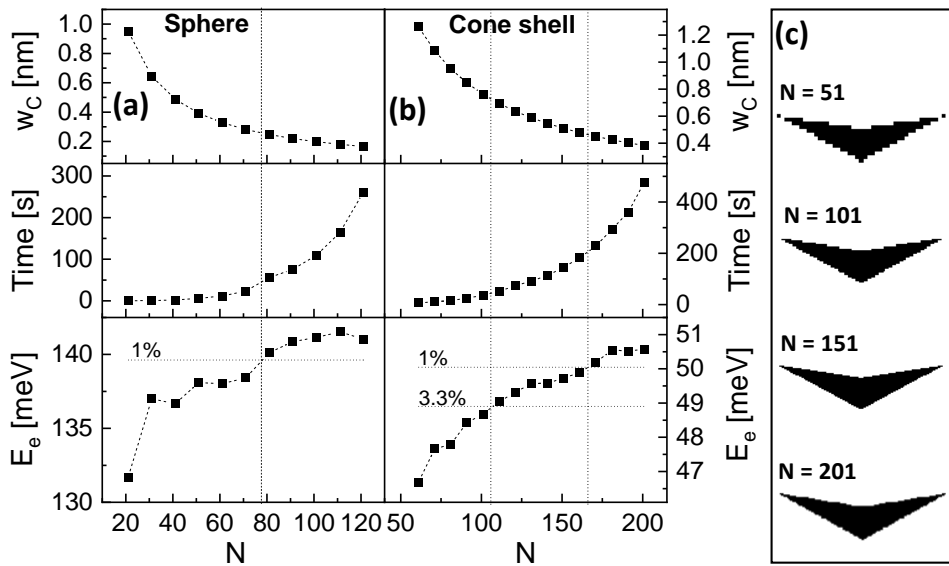


Figure 2. (a) Influence of N on single-particle simulations of a sphere-shaped QD with $r_{QD} = 5 \text{ nm}$ and $w_F = 20 \text{ nm}$. Shown are the width w_C of a mesh-cell, the computation time, and the single-particle energy E_e of the electron ground-state. (b) Influence of N on single-particle simulations of a cone-shell QD with $r_{QD} = 35 \text{ nm}$, $d_{QD} = 19 \text{ nm}$, $h_{QD} = 13.6 \text{ nm}$, and $w_F = 80 \text{ nm}$. In addition, the limits to achieve an accuracy $1 - E_e(N)/E_e(N_{max})$ of 1 % and in (b) of 3.3 % are indicated. (c) Cross-sections through the FEM-mesh of CSQDs with varied N .

without and with a vertical electric field the influence of w_B is very small and the deviation is always below 0.5 % (Fig. 1(d)). These results suggest a value of $w_B \geq 5 \text{ nm}$.

The computation time and the accuracy of the model have an inverse trend. An increased accuracy means a finer meshing which corresponds to a smaller w_C of the mesh cells. When the width w_F of the cubic simulation field is unchanged, this requires a larger N . And, obviously, to solve a larger number of equations takes a longer computation time.

Accordingly, the influence of N on simulations of a sphere-shaped QD and a CSQD is studied (Figs. 2(a) and (b)). To illustrate the FEM-induced discretization, Fig. 2(c) shows cross-sections through CSQDs with varied N . The width of a mesh-cell is given by $w_C = w_F/N$, where $w_F = 20 \text{ nm}$ for the sphere and $w_F = 80 \text{ nm}$ for the CSQD. The computation time depends roughly on N^3 , where simulations on CSQDs are much faster compared to a sphere. This is caused by the larger extend of the probability density in a sphere-shaped QD, which requires a more extensive computation. For both QD shapes, an increasing N yields an increase of E_e . For the sphere, an accuracy $1 - E_e(N)/E_e(N_{max})$ of 1 % is achieved for $N = 78$, $w_C = 0.26 \text{ nm}$, and a computation time of 44 s. For the CSQD, the same accuracy is achieved at $N = 165$, $w_C = 0.46 \text{ nm}$, and a simulation time of 202 s. That means, the larger and more complex cone-shell structure requires a more than four times longer computation time for the same accuracy. For a computation time like that of the sphere-shaped QD, the accuracy is 3.3%, $N = 106$, and $w_C = 0.73 \text{ nm}$.

3.2. Accuracy of multiple-particle corrections

Two multiple-particle corrections are considered in the simulation model. First, the self-consistent charge-carrier correlation and, second, the Coulomb interaction between charge carriers.

For an exciton, the self-consistent correlation correction considers the hole-induced potential for the computation of the electron state and vice versa for the hole (see section 2.3). Due to the doubled number of computation runs, one might expect a doubled computation time for an increase of the number N_{SC} of self-consistent loops from zero (no self-consistent correlation correction) to 1. However, we observe a factor of about 200 for the sphere (Fig. 3(a)) and about 40 for the CSQD (Fig. 3(b)). This clearly indicates the crucial influence

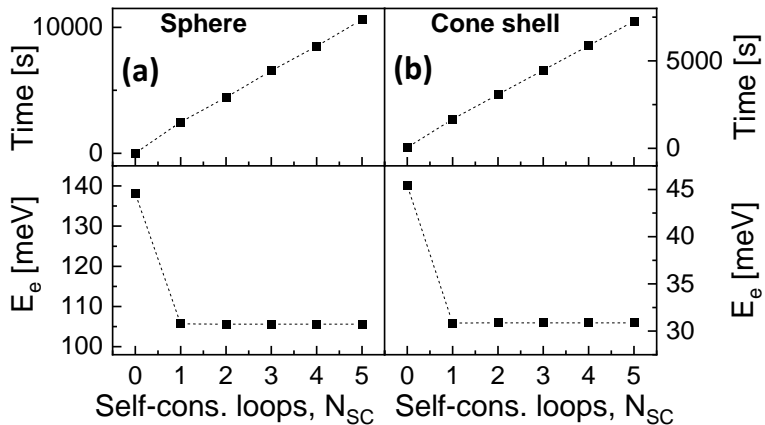


Figure 3. Influence of the number N_{SC} of self-consistent loops for the correlation correction on the computation time and the energy E_e of the electron ground-state energy for (a) a sphere-shaped QD with $r_{QD} = 5$ nm, $N = 51$ and (b) a CSQD with $r_{QD} = 35$ nm, $d_{QD} = 19$ nm, $h_{QD} = 13.6$ nm, and $N = 91$. $N_{SC} = 0$ means no correlation correction.

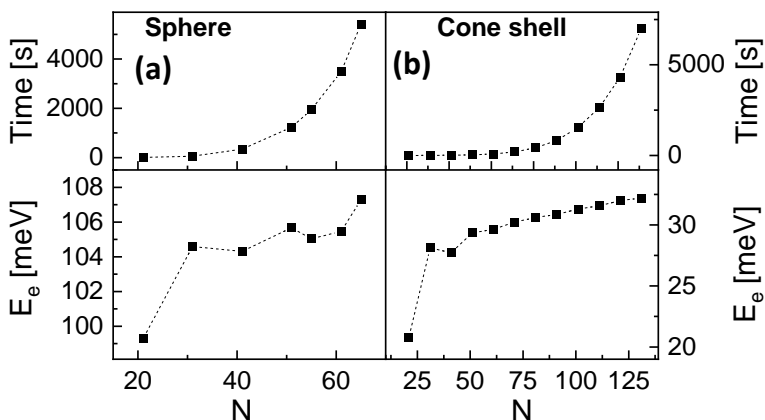


Figure 4. Simulations including the self-assembled correlation correction with $N_{SC} = 1$ and varied N . (a) Sphere-shaped QD with $r_{QD} = 5$ nm. (b) CSQD with $r_{QD} = 35$ nm, $d_{QD} = 19$ nm, $h_{QD} = 13.6$ nm.

of the spatial distribution of the potential on the computation time. Nevertheless, the effect of the correlation correction is pretty large and, thus, represents an important parameter for the simulation. For the sphere-shaped QD we determine a correlation correction of -32.4 meV for the electron ground state and -14.6 meV for the CSQD. Furthermore, the data in Fig. 3 indicate that $N_{SC} = 1$ is enough and larger values yield only negligible further corrections.

Figure 4 establishes that the consideration of self-consistent correlation requires either substantially elongated computation times or a reduced accuracy by using smaller numbers N^3 of FEM mesh cells. In contrast to simulations without correlation correction, even computation times exceeding one hour yield no clear saturation of the simulated E_e with increasing N .

The second multiple-particle correction is the Coulomb interaction which is calculated from the simulated electron and hole wave functions according to Eqn. 2. The numerical solution requires the computation of N^6 individual calculation steps. Therefore, this wave-function analysis is a very time consuming process and we reduce the number of calculation steps by considering only mesh cells where the normalized probability density Ψ/Ψ_{max} is above a cutting value Ψ_{cut} . For instance, a calculation using $\Psi_{cut} = 0.01$ is about 500 times faster compared to a full computation. For a reduction of Ψ_{cut} , the values of C_{eh} saturate and show at $\Psi_{cut} < 0.02$ a deviation of less than 0.1 % from the saturated value.

To summarize this section, the choice of the simulation parameters w_B , N , N_{SC} , and Ψ_{cut} always represents a compromise between computation time and accuracy. With the

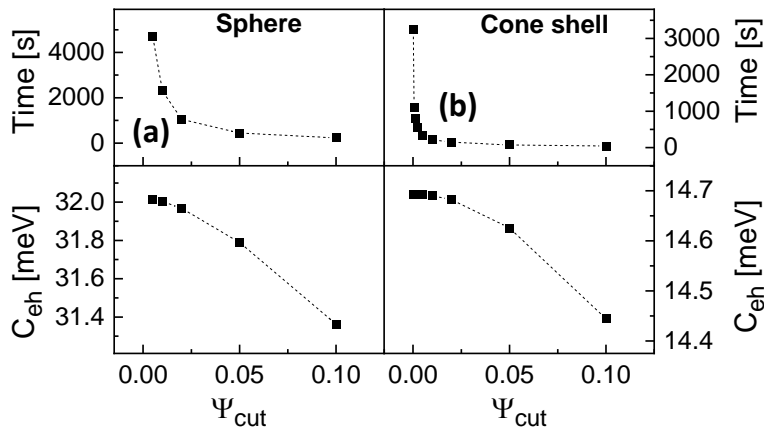


Figure 5. Computation time for the wave-function analysis and resulting Coulomb energy C_{eh} as function of the cutting value Ψ_{cut} , where only mesh cells with normalized probability density above Ψ_{cut} are considered. (a) Sphere-shaped QD with $r_{QD} = 5 \text{ nm}$ and $N = 51$. (b) CSQD with $r_{QD} = 35 \text{ nm}$, $d_{QD} = 19 \text{ nm}$, $h_{QD} = 13.6 \text{ nm}$, and $N = 71$.

recommended values $w_B = 5 \text{ nm}$, $N_{SC} = 1$, and $\Psi_{cut} = 0.02$, the value of N remains as the essential parameter.

4. Examples

We demonstrate the possibilities of the simulation software using CSQDs as an example. CSQDs are promising for applications in quantum information technology [37,38] and their unique shape allows a wide tunability of the charge carrier wave-functions by external electric and magnetic fields [27,28]. The simulation software allows either single simulation runs or series of simulations with one varied parameter. Simulation series are advantageous for instance for an evaluation of the influence of the QD size or of electric or magnetic fields over a wide range.

4.1. Cone-shell quantum dots (CSQDs)

CSQDs are fabricated by filling of a template of droplet-etched nanoholes in AlGaAs with GaAs [7,33]. Accordingly, the cone-like shape of the bottom part of a CSQD is given by the nanohole template and the cone-like indentation on the top by capillarity during hole filling. In the simulation model, the shape is assumed to be rotational symmetric and is defined by three parameters r_{QD} , d_{QD} , and h_{QD} (Fig. 1(b)). During fabrication, the CSQD size can be controlled by the thickness of the GaAs layer deposited for hole filling. With the constant side-facet angle α_B of the droplet etched nanoholes we get the relation $\tan \alpha_B = d_{QD} / r_{QD}$. Typical CSQD sizes determined earlier [27] yield $\tan \alpha_B = 19/35$. Also the side-facet angle α_T of the indentation at the nanohole top is assumed to be constant $\tan \alpha = h_{QD} / r_{QD} = (19 - 13.6)/35$. Now, the size of a CSQD is defined by only one parameter r_{QD} .

Figure 6 shows simulation results for CSQDs with varied size. Here, r_{QD} is varied and h_{QD} , d_{QD} are calculated as is described above. Clearly visible is the decrease of E_X with increasing h_{QD} (fig. 6(a)), which is the well known size quantization effect. The simulation results agree very well with experimental data measured using single-dot photoluminescence (PL) spectroscopy [33]. The Coulomb energy C_{eh} decreases also with increasing h_{QD} (fig. 6(b)), which is caused by the reduced overlap of the electron and hole wave functions in a larger dot. And finally, the splitting $E_X - E_{XX}$ between the exciton and biexciton energy is computed (fig. 6(c)) and shows again a decrease with increasing h_{QD} . A comparison with the experimental data shows a reasonable agreement for smaller CSQDs. On the other side, the simulation computes too small energy splittings for larger dots. Nevertheless, the trend of a decrease of $E_X - E_{XX}$ with increasing dot size is also visible in the experiments.

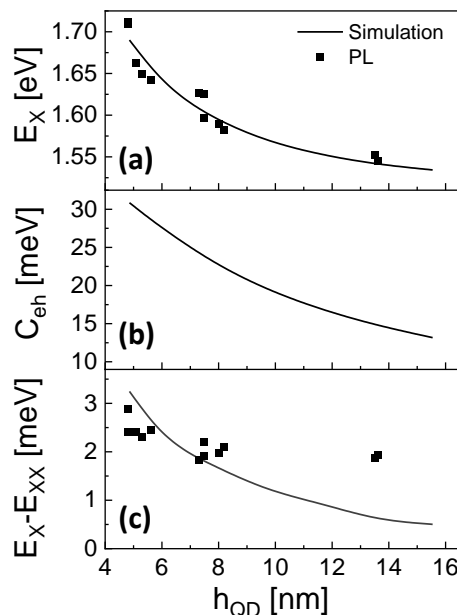


Figure 6. Influence of the size of a CSQD on (a) the exciton energy E_X , (b) the Coulomb energy C_{eh} , and (c) the energy splitting between the exciton and biexciton energy. The simulations are done using $N = 81$, $N_{SC} = 1$, and $\Psi_{cut} = 0.02$. The CSQD size definition is given in the text. In (a) and (c) also experimental results taken using single-dot photoluminescence are shown. The experimental data are taken from [33].

4.2. CSQDs in a uniform electric field

A vertical electric field F_Z modifies the exciton energy according to the well known quantum-confined Stark effect [1,39–43]. A simple approximation assumes the electron and hole probability densities as point charges at a distance p . At zero electric field F we have $p(F = 0) = p_0$. An electric field F yields a charge-carrier separation along field-direction and changes p . With a linear dependence $p(F) = p_0 + \beta F$, the energy shift (Stark shift) becomes parabolic $dE_X(F) = E_X(F) - E_X(F = 0) = -pF + p_0F = -\beta F^2$, with the polarizability β .

Figure 7(a) shows experimental values of E_X in a vertical F_Z [27] where a parabolic Stark shift is clearly visible. The slight asymmetry around $F_Z = 0$ is caused by the asymmetric shape of the CSQD along z-direction. Previous simulations using a two-dimensional (2D) rotation-symmetric model without correlation correction [27] demonstrate a very good reproduction of the experimental Stark shift. The present 3D simulations with $N_{SC} = 0$ agree also well, except a slight deviation around $F_Z = 0$. On the other side, for $N_{SC} = 1$ the values of E_X are strongly reduced by charge-carrier correlation. This correlation-induced deviation of the E_X values indicates that the assumption of the CSQD shape should be corrected. However, this is beyond the scope of the present software related work.

As a significant different in comparison to the experiments and the 2D simulations, the present 3D simulations yield reasonable results only for a limited range of F_Z from -3 MV/m ... 3.5 MV/m. For larger absolute fields, the simulations indicate that either the electron (negative F_Z) or the hole (positive F_Z) probability density residues outside of the dot. This is illustrated in fig. 7(d) for $F_Z = 5$ MV/m. Since the experiments allow larger fields, this seems to be an artifact of the present model. In comparison to a previous 2D model [27], the present 3D model is based on a FEM meshing with cubic cells. The 2D model uses a triangular mesh where the size of the mesh cells is not constant but is dynamically adjusted with respect to the local complexity of the studied structure. This is realized by using the software COMSOL Multiphysics 6.0 (www.comsol.com) for the FEM definition and the solution of the set of partial differential equations [27]. Nevertheless, to

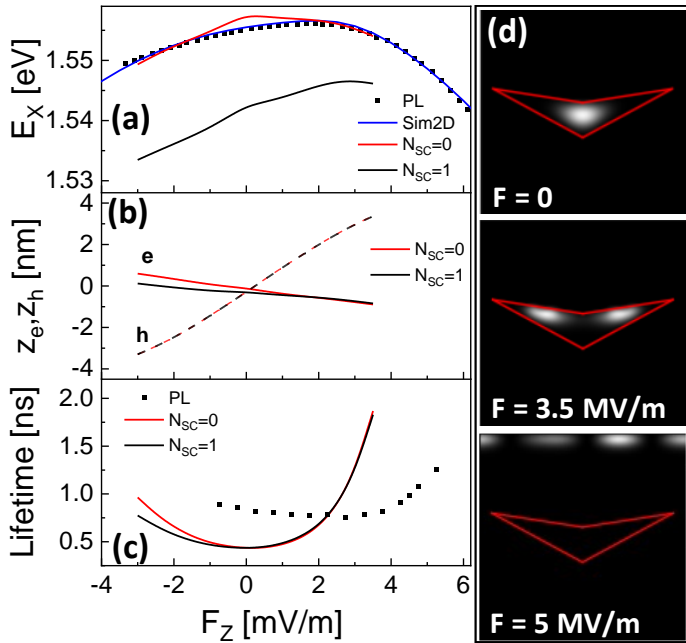


Figure 7. Influence of a vertical electric field F_Z . (a) Exciton energy E_X measured using PL, simulated using a previous 2D model (Sim2D), and simulated using the present 3D model with $r_{QD} = 35$ nm, $d_{QD} = 19$ nm, $h_{QD} = 13.6$ nm, $N = 101$, and either $N_{SC} = 0$ or $N_{SC} = 1$. The experimental data and the results of the 2D simulations are taken from ref. [27]. (b) Simulated z-positions of the electron and hole barycenters. (c) Measured and simulated radiative lifetime. The experimental data are taken from ref. [29]. (d) Cross-sectional hole probability densities for $N = 101$, $N_{SC} = 1$, and at varied F_Z . The red lines mark the CSQD shape.

provide an open-source and fully Python-based simulation software, we stick to the cubic meshing, at this stage.

In fig. 7(b) the z -positions of the electron and hole barycenters are plotted as function of F_Z . Clearly visible is the field-driven shift of the charge carriers, where simulations with and without correlation correction show an only small deviation for electrons and are identical for holes. The charge-carrier shift is much stronger for the hole in comparison to the electron. Due to its higher effective mass, the hole is more squeezed into the QD shape and, thus, can be shifted more easily by an external electric field. This identifies the hole to be more interesting for a manipulation by an external electric field.

A negative F_Z shifts the hole towards the tip at the bottom of a CSQD and a positive F_Z towards the wing part at the top. Since the CSQD top part has an indentation, the hole probability density at high positive F_Z is transformed into a quantum ring with tunable radius. This is illustrated in Fig. 7(d) at $F_Z = 3.5$ MV/m and already predicted in previous publications [27]. Quantum rings in general are highly attractive quantum structures with intriguing properties [44] and for CSQDs in combined electric and magnetic fields an application as storage for photo-excited charge carriers is predicted [28]. This topic will be addressed below in section 4.4.

Figure 7(c) compares the simulated and measured radiative lifetimes in a CSQD at varied F_Z . We attribute the significant deviation to an interesting physical effect. The simulations assume the usual strong confinement regime for the calculation of the lifetime (Eqn. 7 in section 2.4). This approach is assumed when the QD size is smaller than the bulk exciton Bohr radius λ_B [35,36,45–47]. However, the radius of the hole probability density in the ring state exceeds λ_B and the confinement is now weak with a significantly reduced lifetime. Here, a charge carrier can oscillate and collect a substantially higher recombination probability [48,49]. For the present CSQD at high F_Z , we assume a novel asymmetric confinement, which is weak for the hole and strong for the electron. In this sense, the

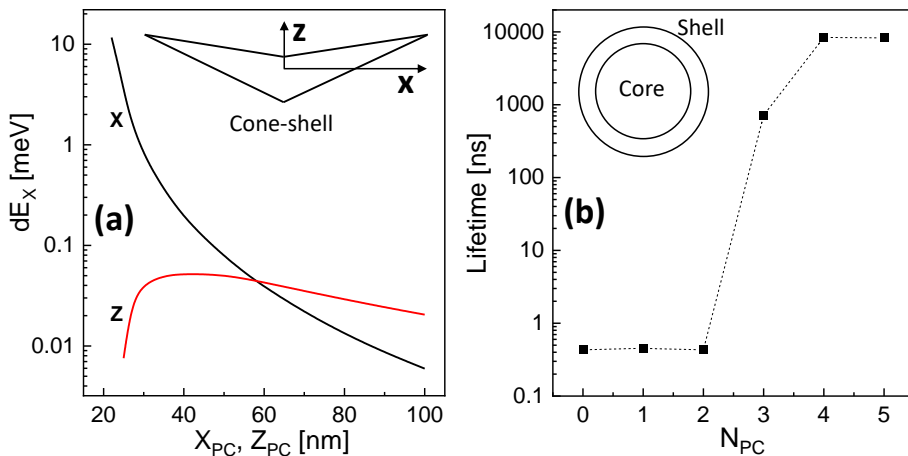


Figure 8. (a) Shift of E_X (equivalent to the optical linewidth) induced by a point charge in a lateral distance x_{PC} (black line) or a vertical distance z_{PC} (red line) to the center of a CSQD ($z = 0$ is at $d_{QD}/2$). The simulations are done using $r_{QD} = 35$ nm, $d_{QD} = 19$ nm, $h_{QD} = 13.6$ nm, $N = 81$, $N_{SC} = 1$, and $\Psi_{cut} = 0.02$. (b) Radiative exciton lifetime of a GaAs/AlGaAs core-shell QD with a core radius of 5 nm as function of the number N_{PC} of point charges located at a distance of 7 nm (surface of the shell) from the QD center. The simulations are done using $N = 51$, $N_{SC} = 1$, and $\Psi_{cut} = 0.02$.

discrepancy between simulated and experimental lifetimes represents a confirmation for the predicted transformation of the hole from a dot into a quantum ring.

Finally, also simulations in a lateral electric field F_X are possible. A strong F_X separates the electron and hole laterally and forms an in-plane electric dipole, where the orientation is controlled by the direction of the lateral field. This topic is intensively studied in a previous publication [30] and not further addressed here.

4.3. CSQDs in the field of point charges

An ultra-narrow emission linewidth is essential for the usage of a QD, e.g., for the generation of indistinguishable photons for quantum cryptography [12] or for resonant coupling into Rb atoms for light storage [11]. The minimum optical linewidth Γ_0 can be estimated from Heisenberg's uncertainty principle $\tau\Gamma_0 \geq \hbar/2$. For a typical QD radiative lifetime $\tau \simeq 0.5$ ns this natural linewidth becomes $\Gamma_0 = 0.6$ μ eV. However, measurements often show much broader lines. An important source of noise that can broaden single-dot PL peaks is the charge noise [50,51]. Charge noise is caused by fluctuating charges in the surrounding of the dot which yield a time-dependent electric field and, thus, a fluctuating QD emission energy by the quantum-confined Stark effect (see section 4.2). For epitaxial QDs, charge noise is also called spectral diffusion [52,53] and the charges are located in crystal traps in the barrier material around the dots. In this definition, a trap is a crystal defect which can be either neutral or populated by a point charge. PL experiments on single QDs usually integrate over measurement times of seconds and, thus, average over situations with different populations of the traps and correspondingly different emission energies.

For an evaluation of this topic, the difference of the exciton energies with and without a point charge is taken as the optical line width [54]. Figure 8(a) shows examples where a single point-charge is assumed either in x- or in z-direction. The simulation results illustrate that an exciton linewidth below e.g. 10 μ eV requires distances d_T of the trap larger than 100 nm. The trap distance d_T can be transformed into a trap density N_T using a rough estimation $N_T = 1/(2d_T)^3$, where a periodic lattice with lattice constant $2d_T$ is assumed. Now, the above condition $dE_x < 10$ μ eV requires ultra-pure crystals with a trap density N_T below 10^{14} cm⁻³. Furthermore, Fig. 8(a) demonstrates that not only the distance but also the direction of a point charge plays a role.

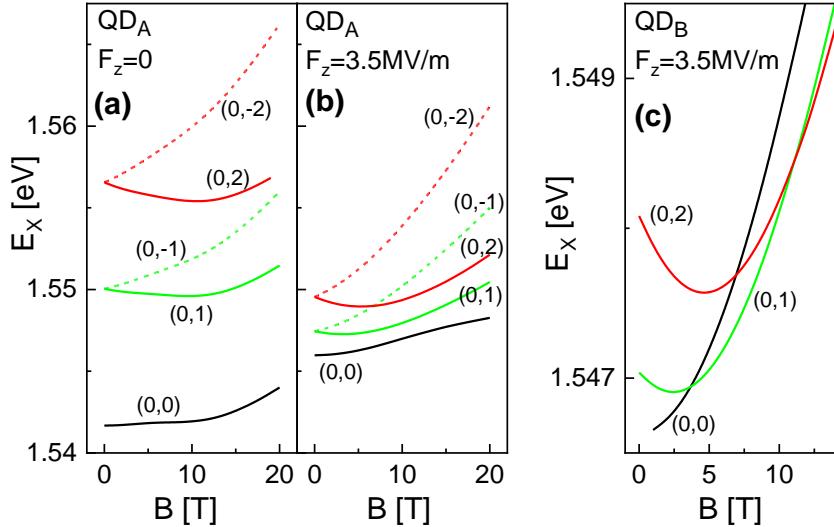


Figure 9. (a) B -dependence of E_X for a CSQD with $r_{QD} = 35$ nm, $d_{QD} = 19$ nm, $h_{QD} = 13.6$ nm (QD_A). The vertical electric field is $F_z = 0$ and L_h is varied. The respective values of (L_e, L_h) are indicated. The simulations are done using $N = 81$, $N_{SC} = 1$, and $\Psi_{cut} = 0.02$. (b) B -dependence of E_X for QD_A and $F_z = 3.5$ MV/m. (c) B -dependence of E_X for QD_B with modified $d_{QD} = 25$ nm and $F_z = 3.5$ MV/m.

Colloidal core-shell QDs [1] are composed of a core with a low-bandgap semiconductor which is surrounded by a shell of a semiconductor with a larger bandgap. The whole core shell QD is usually embedded in a matrix of ligands. A major issue for the optical properties is the so-called blinking [55]. Blinking means an abrupt energy shift or an on/off switching of the optical emission, where often non-radiative Auger recombinations are assumed as origin [55]. An alternative explanation is demonstrated in Figure 8(b). There a spherically shaped GaAs QD with $r_{QD} = 5$ nm is simulated, which is surrounded by AlGaAs as an approximation of a shell. A number of N_{PC} point charges is located at a distance of 7 nm from the QD center, which represents the surface of a 2 nm thick shell and, thus, the shell-ligand interface. For N_{PC} up to two, the simulated lifetime $\tau \simeq 0.44$ ns is approximately constant, whereas for larger N_{PC} the lifetime increases almost abruptly by more than 4 orders of magnitude. For such long lifetimes only negligible optical recombination is expected. Accordingly, for a QD with $N_{PC} = 1$, a fluctuating occupation of a second trap will cause an energy shift and the occupation of a third trap an on/off switching (blinking) of the optical emission.

4.4. CSQDs in a magnetic field

A magnetic field splits the quantized energy levels of charge carriers confined in a QD [56–61] analogous to the Zeeman-splitting of atomic spectral lines. This is often described analytically by the Fock-Darwin model [62] which assumes a parabolic confinement and introduces the angular momentum quantum number L . Since optically active QDs provide a confinement for electrons and holes, the B -field dependence of the optical emission is controlled by the angular momentum quantum numbers of both, the electron L_e and the hole L_h . Here, selection rules require for optical transitions that $L_e = L_h$.

We start the B -dependent simulations with a CSQD (QD_A) which is already discussed in sections 4.2 and 4.3. Figure 9(a) shows the B -dependence of E_X for $F_z = 0$ and varied L_h . The results agree qualitatively with the predictions of the Fock-Darwin model. At zero electric field, the shape of the electron and hole probability densities is close to a sphere, which is consistent with the parabolic confinement assumed in the Fock-Darwin model. For $F_z = 3.5$ MV/m, we see a significant change of the exciton energies (Fig. 9(b)). Now, the vertical electric field pushes the hole into the wing part of the CSQD, where it forms a quantum ring (Fig. 7(d), section 4.2). The ground state with $(L_e, L_h) = (0,0)$ is elevated by an increasing F_z , which is already observed in Fig. 7(a). However, the level spacing between

the ground and the excited states ($|L_e|$ or $|L_h| > 0$) is strongly reduced and the slope of the B -dependence is modified. In the next step, the shape of the CSQD is modified and d_{QD} is enhanced from 19 nm to 25 nm (QD_B). Now, the B -dependence demonstrates an interesting effect at higher B , where excited states with $L_h > 0$ become the lowest-energy state E_{X0} . Such transitions are predicted at $B = 3.6$ T ($L_h = 0$ to 1) and $B = 11.4$ T ($L_h = 1$ to 2). Additional simulations indicate that E_{X0} always includes an electron with a zero L_e . With the selection rule that optical transitions between electrons and holes require $L_e = L_h$, only states with $L_h = 0$ can be optically active. Accordingly, the transition at $B = 3.6$ T from $L_h = 0$ to 1 is equivalent with a bright to dark transition. Alternatively the bright to dark transition can be triggered by a change of F_z . For conditions with a low excitation power where only the ground-state of the CSQD is occupied, the bright to dark transition can provide a mechanism for a controlled storage of photoexcited charge carriers [28]. Such a switching between bright and dark exciton ground states by a B -field was theoretically predicted assuming an idealized quantum ring shape [63,64]. Here, we predict this effect for a structure that can probably be realized experimentally.

Furthermore, the B -dependence of the lowest-energy state E_{X0} in Fig. 9(c) shows an oscillatory behavior. Magnetic-field dependent oscillations of the energy levels of charge carriers in a quantum ring are well known as Aharonov-Bohm oscillations [65] and related to quantum-interference phenomena. But Aharonov-Bohm oscillations are usually observed for charged particles and not expected for neutral excitons. However, the strong F_z -induced polarization in the presents CSQDs provides a significant charge-carrier separation and allows the excitonic oscillations of E_{X0} in Fig. 9(c) [63,64,66–68].

5. Conclusions

The discussed Python-based open-source 3D simulation software (<https://github.com/HappyCodingz/PyDotSim>) represents a powerful tool for the evaluation of the optical emission from semiconductor QDs. The consideration of Coulomb interaction and correlation in a self-consistent fashion allows the simulation also of multiple-particle systems like excitons and biexcitons. An important aspect is the influence of external uniform electric and magnetic fields and the field induced by point-charges. Discussed examples like the QD size dependence of the exciton energy and the exciton-biexciton splitting, the influence of a vertical electric field with a strong Stark-shift, a dot to ring transformation of the hole, and a novel strong-weak confinement regime, the influence of point charges on the linewidth of the exciton peak and on the blinking, the possibility to store photoexcited charge carriers in a combined electric and magnetic field, and the possibility of optical Aharonov-Bohm oscillations demonstrate the capabilities of the simulation tool. The convenient usage suggests the simulation tool for education and for experimenters who wants to predict or evaluate their experimental findings.

Author Contributions: Conceptualization, C.H.; methodology, C.H.; software, C.H.; validation, C.H.; formal analysis, C.H.; investigation, C.H.; resources, C.H.; data curation, C.H.; writing—original draft preparation, C.H.; writing—review and editing, C.H.; visualization, C.H.; supervision, C.H.; project administration, C.H.; funding acquisition, C.H.. All authors have read and agreed to the published version of the manuscript.

Funding: This research received funding from the “Deutsche Forschungsgemeinschaft” via HE 2466/2-1.

Acknowledgments: The author thanks Carlos A. Duque, Geoffrey Pirard, Gabriel Bester, and Wolfgang Hansen for stimulating and motivating discussions, and the “Deutsche Forschungsgemeinschaft” for financial support.

Conflicts of Interest: The author declares no conflict of interest.

References

1. Empedocles, S.A.; Bawendi, M.G. Quantum-Confining Stark Effect in Single CdSe Nanocrystallite Quantum Dots. *Science* **1997**, *278*, 2114–2117. <https://doi.org/10.1126/science.278.5346.211>.
2. Koguchi, N.; Takahashi, S.; Chikyow, T. New MBE growth method for InSb quantum well boxes. *Journal of Crystal Growth* **1991**, *111*, 688–692. [https://doi.org/10.1016/0022-0248\(91\)91064-H](https://doi.org/10.1016/0022-0248(91)91064-H).
3. Leonard, D.; Krishnamurthy, M.; Fafard, S.; Merz, J.L.; Petroff, P.M. Molecular-beam epitaxy growth of quantum dots from strained coherent uniform islands of InGaAs on GaAs. *Journal of Vacuum Science & Technology B: Microelectronics and Nanometer Structures Processing, Measurement, and Phenomena* **1994**, *12*, 1063–1066. Publisher: American Institute of Physics, <https://doi.org/10.1116/1.587088>.
4. Madhukar, A.; Xie, Q.; Chen, P.; Konkar, A. Nature of strained InAs three-dimensional island formation and distribution on GaAs(100). *Applied Physics Letters* **1994**, *64*, 2727–2729. Publisher: American Institute of Physics, <https://doi.org/10.1063/1.111456>.
5. Moison, J.M.; Houzay, F.; Barthe, F.; Leprince, L.; André, E.; Vatet, O. Self-organized growth of regular nanometer-scale InAs dots on GaAs. *Applied Physics Letters* **1994**, *64*, 196–198. Publisher: American Institute of Physics, <https://doi.org/10.1063/1.111502>.
6. Mano, T.; Watanabe, K.; Tsukamoto, S.; Koguchi, N.; Fujioka, H.; Oshima, M.; Lee, C.D.; Leem, J.Y.; Lee, H.J.; Noh, S.K. Nanoscale InGaAs concave disks fabricated by heterogeneous droplet epitaxy. *Applied Physics Letters* **2000**, *76*, 3543–3545. <https://doi.org/10.1063/1.126701>.
7. Heyn, C.; Stemmann, A.; Köppen, T.; Strelow, C.; Kipp, T.; Grave, M.; Mendach, S.; Hansen, W. Highly uniform and strain-free GaAs quantum dots fabricated by filling of self-assembled nanoholes. *Applied Physics Letters* **2009**, *94*, 183113–183115. <https://doi.org/10.1063/1.3133338>.
8. Bietti, S.; Bocquel, J.; Adorno, S.; Mano, T.; Keizer, J.G.; Koenraad, P.M.; Sanguinetti, S. Precise shape engineering of epitaxial quantum dots by growth kinetics. *Physical Review B* **2015**, *92*, 075425. <https://doi.org/10.1103/PhysRevB.92.075425>.
9. Gajjela, R.S.R.; Koenraad, P.M. Atomic-Scale Characterization of Droplet Epitaxy Quantum Dots. *Nanomaterials* **2021**, *11*, 85. Number: 1 Publisher: Multidisciplinary Digital Publishing Institute, <https://doi.org/10.3390/nano11010085>.
10. Vasconcellos, S.M.d.; Gordon, S.; Bichler, M.; Meier, T.; Zrenner, A. Coherent control of a single exciton qubit by optoelectronic manipulation. *Nature Photonics* **2010**, *4*, 545–548. <https://doi.org/10.1038/nphoton.2010.124>.
11. Akopian, N.; Wang, L.; Rastelli, A.; Schmidt, O.G.; Zwiller, V. Hybrid semiconductor-atomic interface: slowing down single photons from a quantum dot. *Nature Photonics* **2011**, *5*, 230–233. <https://doi.org/10.1038/nphoton.2011.16>.
12. Müller, M.; Bounouar, S.; Jöns, K.D.; Glässl, M.; Michler, P. On-demand generation of indistinguishable polarization-entangled photon pairs. *Nature Photonics* **2014**, *8*, 224–228. <https://doi.org/10.1038/nphoton.2013.377>.
13. Lodahl, P.; Mahmoodian, S.; Stobbe, S. Interfacing single photons and single quantum dots with photonic nanostructures. *Reviews of Modern Physics* **2015**, *87*, 347–400. <https://doi.org/10.1103/RevModPhys.87.347>.
14. Lodahl, P.; Ludwig, A.; Warburton, R.J. A deterministic source of single photons. *Physics Today* **2022**, *75*, 44–50. <https://doi.org/10.1063/PT.3.4962>.
15. Vajner, D.A.; Rickert, L.; Gao, T.; Kaymazlar, K.; Heindel, T. Quantum Communication Using Semiconductor Quantum Dots. *Advanced Quantum Technologies* **2022**, *5*, 2100116. _eprint: <https://onlinelibrary.wiley.com/doi/pdf/10.1002/qute.202100116>, <https://doi.org/10.1002/qute.202100116>.
16. Luo, W.; Cao, L.; Shi, Y.; Wan, L.; Zhang, H.; Li, S.; Chen, G.; Li, Y.; Li, S.; Wang, Y.; et al. Recent progress in quantum photonic chips for quantum communication and internet. *Light: Science & Applications* **2023**, *12*, 175. Publisher: Nature Publishing Group, <https://doi.org/10.1038/s41377-023-01173-8>.
17. Bester, G.; Nair, S.; Zunger, A. Pseudopotential calculation of the excitonic fine structure of million-atom self-assembled $\{\mathrm{In}\}_{\{1\}}\mathrm{x}\{\mathrm{Ga}\}_{\{x\}}\mathrm{A}\}$ quantum dots. *Physical Review B* **2003**, *67*, 161306. Publisher: American Physical Society, <https://doi.org/10.1103/PhysRevB.67.161306>.
18. Bester, G. Electronic excitations in nanostructures: an empirical pseudopotential based approach. *Journal of Physics: Condensed Matter* **2008**, *21*, 023202. Publisher: IOP Publishing, <https://doi.org/10.1088/0953-8984/21/2/023202>.

19. Baraff, G.A.; Gershoni, D. Eigenfunction-expansion method for solving the quantum-wire problem: Formulation. *Physical Review B* **1991**, *43*, 4011–4022. Publisher: American Physical Society, <https://doi.org/10.1103/PhysRevB.43.4011>. 499
500
501
20. Stier, O.; Grundmann, M.; Bimberg, D. Electronic and optical properties of strained quantum dots modeled by 8-band $k\backslash\text{ensuremath}\{\cdot\backslash\text{cdot}\}p$ theory. *Physical Review B* **1999**, *59*, 5688–5701. 502
503
504
<https://doi.org/10.1103/PhysRevB.59.5688>.
21. Seguin, R.; Schliwa, A.; Rodt, S.; Pötschke, K.; Pohl, U.W.; Bimberg, D. Size-Dependent Fine-Structure Splitting in Self-Organized InAs/GaAs Quantum Dots. *Physical Review Letters* **2005**, *95*, 257402. Publisher: American Physical Society, <https://doi.org/10.1103/PhysRevLett.95.257402>. 505
506
507
508
22. Graf, A.; Sonnenberg, D.; Paulava, V.; Schliwa, A.; Heyn, C.; Hansen, W. Excitonic states in GaAs quantum dots fabricated by local droplet etching. *Physical Review B* **2014**, *89*, 115314. 509
510
511
<https://doi.org/10.1103/PhysRevB.89.115314>.
23. Melnik, R.V.N.; Willatzen, M. Bandstructures of conical quantum dots with wetting layers. *Nanotechnology* **2004**, *15*, 1. <https://doi.org/10.1088/0957-4484/15/1/001>. 512
513
24. Grundmann, M.; Stier, O.; Bimberg, D. InAs/GaAs pyramidal quantum dots: Strain distribution, optical phonons, and electronic structure. *Physical Review B* **1995**, *52*, 11969–11981. Publisher: American Physical Society, <https://doi.org/10.1103/PhysRevB.52.11969>. 514
515
516
25. Bester, G.; Zunger, A. Cylindrically shaped zinc-blende semiconductor quantum dots do not have cylindrical symmetry: Atomistic symmetry, atomic relaxation, and piezoelectric effects. *Physical Review B* **2005**, *71*, 045318. Publisher: American Physical Society, <https://doi.org/10.1103/PhysRevB.71.045318>. 517
518
519
520
26. Huo, Y.H.; Rastelli, A.; Schmidt, O.G. Ultra-small excitonic fine structure splitting in highly symmetric quantum dots on GaAs (001) substrate. *Applied Physics Letters* **2013**, *102*, 152105–152108. <https://doi.org/10.1063/1.4802088>. 521
522
523
27. Heyn, C.; Ranasinghe, L.; Deneke, K.; Alshaikh, A.; Duque, C.A.; Hansen, W. Strong Electric Polarizability of Cone–Shell Quantum Structures for a Large Stark Shift, Tunable Long Exciton Lifetimes, and a Dot-to-Ring Transformation. *Nanomaterials* **2023**, *13*, 857. Number: 5 Publisher: Multidisciplinary Digital Publishing Institute, <https://doi.org/10.3390/nano13050857>. 524
525
526
527
28. Heyn, C.; Ranasinghe, L.; Alshaikh, A.; Duque, C.A. Cone–Shell Quantum Structures in Electric and Magnetic Fields as Switchable Traps for Photoexcited Charge Carriers. *Nanomaterials* **2023**, *13*, 1696. Number: 10 Publisher: Multidisciplinary Digital Publishing Institute, <https://doi.org/10.3390/nano13101696>. 528
529
530
531
29. Alshaikh, A.; Peng, J.; Zierold, R.; Blick, R.H.; Heyn, C. Vertical Electric-Field-Induced Switching from Strong to Asymmetric Strong–Weak Confinement in GaAs Cone–Shell Quantum Dots Using Transparent Al-Doped ZnO Gates. *Nanomaterials* **2024**, *14*, 1712. Number: 21 Publisher: Multidisciplinary Digital Publishing Institute, <https://doi.org/10.3390/nano14211712>. 532
533
534
535
30. Alshaikh, A.; Blick, R.H.; Heyn, C. GaAs Cone–Shell Quantum Dots in a Lateral Electric Field: Exciton Stark-Shift, Lifetime, and Fine-Structure Splitting. *Nanomaterials* **2024**, *14*, 1174. Number: 14 Publisher: Multidisciplinary Digital Publishing Institute, <https://doi.org/10.3390/nano1411174>. 536
537
538
539
31. Harrison, P.; Valavanis, A. *Quantum Wells, Wires and Dots*, 4 ed.; Theoretical and Computational Physics of Semiconductor Nanostructures, Wiley-VCH, 2016. 540
541
32. Vurgaftman, I.; Meyer, J.R.; Ram-Mohan, L.R. Band parameters for III–V compound semiconductors and their alloys. *Journal of Applied Physics* **2001**, *89*, 5815–5875. <https://doi.org/10.1063/1.1368156>. 542
543
544
33. Heyn, C.; Gräfenstein, A.; Pirard, G.; Ranasinghe, L.; Deneke, K.; Alshaikh, A.; Bester, G.; Hansen, W. Dot-Size Dependent Excitons in Droplet-Etched Cone–Shell GaAs Quantum Dots. *Nanomaterials* **2022**, *12*, 2981. <https://doi.org/10.3390/nano12172981>. 545
546
547
34. Narvaez, G.A.; Bester, G.; Franceschetti, A.; Zunger, A. Excitonic exchange effects on the radiative decay time of monoexcitons and biexcitons in quantum dots. *Physical Review B* **2006**, *74*, 205422. Publisher: American Physical Society, <https://doi.org/10.1103/PhysRevB.74.205422>. 548
549
550
551
35. Tighineanu, P.; Daveau, R.; Lee, E.H.; Song, J.D.; Stobbe, S.; Lodahl, P. Decay dynamics and exciton localization in large GaAs quantum dots grown by droplet epitaxy. *Physical Review B* **2013**, *88*, 155320. Publisher: American Physical Society, <https://doi.org/10.1103/PhysRevB.88.155320>. 552
553
554
555
36. Dalgarno, P.A.; Smith, J.M.; McFarlane, J.; Gerardot, B.D.; Karrai, K.; Badolato, A.; Petroff, P.M.; Warburton, R.J. Coulomb interactions in single charged self-assembled quantum dots: 556
557

- Radiative lifetime and recombination energy. *Physical Review B* **2008**, *77*, 245311. <https://doi.org/10.1103/PhysRevB.77.245311>. 558
559
37. Zhai, L.; Löbl, M.C.; Nguyen, G.N.; Ritzmann, J.; Javadi, A.; Spinnler, C.; Wieck, A.D.; Ludwig, A.; Warburton, R.J. Low-noise GaAs quantum dots for quantum photonics. *Nature Communications* **2020**, *11*, 4745. Number: 1 Publisher: Nature Publishing Group, <https://doi.org/10.1038/s41467-020-18625-z>. 560
561
562
563
38. Zhai, L.; Nguyen, G.N.; Spinnler, C.; Ritzmann, J.; Löbl, M.C.; Wieck, A.D.; Ludwig, A.; Javadi, A.; Warburton, R.J. Quantum interference of identical photons from remote GaAs quantum dots. *Nature Nanotechnology* **2022**, *17*, 829–833. Publisher: Nature Publishing Group, <https://doi.org/10.1038/s41565-022-01131-2>. 564
565
566
567
39. Mendez, E.; Bastard, G.; Chang, L.; Esaki, L.; Morkoc, H.; Fischer, R. Effect of an electric field on the luminescence of GaAs quantum wells. *Physical Review B* **1982**, *26*, 7101–7104. <https://doi.org/10.1103/PhysRevB.26.7101>. 568
569
570
40. Miller, D.A.B.; Chemla, D.S.; Damen, T.C.; Gossard, A.C.; Wiegmann, W.; Wood, T.H.; Burrus, C.A. Band-Edge Electroabsorption in Quantum Well Structures: The Quantum-Confinement Stark Effect. *Physical Review Letters* **1984**, *53*, 2173–2176. Publisher: American Physical Society, <https://doi.org/10.1103/PhysRevLett.53.2173>. 571
572
573
574
41. Heller, W.; Bockelmann, U.; Abstreiter, G. Electric-field effects on excitons in quantum dots. *Physical Review B* **1998**, *57*, 6270–6273. Publisher: American Physical Society, <https://doi.org/10.1103/PhysRevB.57.6270>. 575
576
577
42. Finley, J.J.; Sabathil, M.; Vogl, P.; Abstreiter, G.; Oulton, R.; Tartakovskii, A.I.; Mowbray, D.J.; Skolnick, M.S.; Liew, S.L.; Cullis, A.G.; et al. Quantum-confined Stark shifts of charged exciton complexes in quantum dots. *Physical Review B* **2004**, *70*, 201308. <https://doi.org/10.1103/PhysRevB.70.201308>. 578
579
580
581
43. Bennett, A.J.; Patel, R.B.; Joanna, S.S.; Christine A., N.; David A., F.; Andrew J., S. Giant Stark effect in the emission of single semiconductor quantum dots. *Applied Physics Letter* **2010**, *97*, 031104. 582
583
584
44. Fomin, V.M., Ed. *Physics of Quantum Rings*; NanoScience and Technology, Springer International Publishing: Cham, 2018. <https://doi.org/10.1007/978-3-319-95159-1>. 585
586
45. Giessen, H.; Woggon, U.; Fluegel, B.; Mohs, G.; Hu, Y.Z.; Koch, S.W.; Peyghambarian, N. Quantum dots in the strong confinement regime: a model system for gain in quasi zero-dimensional semiconductors. *Chemical Physics* **1996**, *210*, 71–78. [https://doi.org/10.1016/0301-0104\(96\)00193-0](https://doi.org/10.1016/0301-0104(96)00193-0). 587
588
589
590
46. Okuno, T.; Lipovskii, A.A.; Ogawa, T.; Amagai, I.; Masumoto, Y. Strong confinement of PbSe and PbS quantum dots. *Journal of Luminescence* **2000**, *87-89*, 491–493. [https://doi.org/10.1016/S0022-2313\(99\)00220-3](https://doi.org/10.1016/S0022-2313(99)00220-3). 591
592
593
47. Ning, J.Q.; Zheng, C.C.; Zhang, X.H.; Xu, S.J. Strong quantum confinement effect and reduced Fröhlich exciton–phonon coupling in ZnO quantum dots embedded inside a SiO₂ matrix. *Nanoscale* **2015**, *7*, 17482–17487. Publisher: The Royal Society of Chemistry, <https://doi.org/10.1039/C5NR04520G>. 594
595
596
597
48. Stobbe, S.; Schlereth, T.W.; Höfling, S.; Forchel, A.; Hvam, J.M.; Lodahl, P. Large quantum dots with small oscillator strength. *Physical Review B* **2010**, *82*, 233302. Publisher: American Physical Society, <https://doi.org/10.1103/PhysRevB.82.233302>. 598
599
600
49. Stobbe, S.; Kristensen, P.T.; Mortensen, J.E.; Hvam, J.M.; Mørk, J.; Lodahl, P. Spontaneous emission from large quantum dots in nanostructures: Exciton-photon interaction beyond the dipole approximation. *Physical Review B* **2012**, *86*, 085304. Publisher: American Physical Society, <https://doi.org/10.1103/PhysRevB.86.085304>. 601
602
603
604
50. Kuhlmann, A.V.; Houel, J.; Ludwig, A.; Greuter, L.; Reuter, D.; Wieck, A.D.; Poggio, M.; Warburton, R.J. Charge noise and spin noise in a semiconductor quantum device. *Nature Physics* **2013**, *9*, 570. <https://doi.org/10.1038/nphys2688>. 605
606
607
51. Matthiesen, C.; Vamivakas, A.N.; Atatüre, M. Subnatural Linewidth Single Photons from a Quantum Dot. *Physical Review Letters* **2012**, *108*, 093602. <https://doi.org/10.1103/PhysRevLett.108.093602>. 608
609
610
52. Seufert, J.; Weigand, R.; Bacher, G.; Kümmell, T.; Forchel, A.; Leonardi, K.; Hommel, D. Spectral diffusion of the exciton transition in a single self-organized quantum dot. *Applied Physics Letters* **2000**, *76*, 1872–1874. <https://doi.org/10.1063/1.126196>. 611
612
613
53. Abbarchi, M.; Troiani, F.; Mastrandrea, C.; Goldoni, G.; Kuroda, T.; Mano, T.; Sakoda, K.; Koguchi, N.; Sanguinetti, S.; Vinattieri, A.; et al. Spectral diffusion and line broadening in single 614
615

- self-assembled GaAs/AlGaAs quantum dot photoluminescence. *Applied Physics Letters* **2008**, *93*, 162101. <https://doi.org/10.1063/1.3003578>. 616
617
54. Heyn, C.; Ranasinghe, L.; Zocher, M.; Hansen, W. Shape-Dependent Stark Shift and Emission-Line Broadening of Quantum Dots and Rings. *The Journal of Physical Chemistry C* **2020**, *124*, 19809–19816. Publisher: American Chemical Society, <https://doi.org/10.1021/acs.jpcc.0c05043>. 618
619
620
55. Efros, A.L.; Nesbitt, D.J. Origin and control of blinking in quantum dots. *Nature Nanotechnology* **2016**, *11*, 661–671. <https://doi.org/10.1038/nnano.2016.140>. 621
622
56. Maksym, P.A.; Chakraborty, T. Quantum dots in a magnetic field: Role of electron-electron interactions. *Physical Review Letters* **1990**, *65*, 108–111. Publisher: American Physical Society, <https://doi.org/10.1103/PhysRevLett.65.108>. 623
624
625
57. Halonen, V.; Chakraborty, T.; Pietiläinen, P. Excitons in a parabolic quantum dot in magnetic fields. *Physical Review B* **1992**, *45*, 5980–5985. Publisher: American Physical Society, <https://doi.org/10.1103/PhysRevB.45.5980>. 626
627
628
58. Kouwenhoven, L.P.; Austing, D.G.; Tarucha, S. Few-electron quantum dots. *Reports on Progress in Physics* **2001**, *64*, 701–736. Publisher: IOP Publishing, <https://doi.org/10.1088/0034-4885/64/6/201>. 629
630
631
59. Dreiser, J.; Atatüre, M.; Galland, C.; Müller, T.; Badolato, A.; Imamoglu, A. Optical investigations of quantum dot spin dynamics as a function of external electric and magnetic fields. *Physical Review B* **2008**, *77*, 075317. Publisher: American Physical Society, <https://doi.org/10.1103/PhysRevB.77.075317>. 632
633
634
635
60. Jahan, K.L.; Boda, A.; Shankar, I.V.; Raju, C.N.; Chatterjee, A. Magnetic field effect on the energy levels of an exciton in a GaAs quantum dot: Application for excitonic lasers. *Scientific Reports* **2018**, *8*, 5073. Number: 1 Publisher: Nature Publishing Group, <https://doi.org/10.1038/s41598-018-23348-9>. 636
637
638
639
61. Heyn, C.; Duque, C.A. Donor impurity related optical and electronic properties of cylindrical GaAs-AlGaAs quantum dots under tilted electric and magnetic fields. *Scientific Reports* **2020**, *10*, 9155. Number: 1 Publisher: Nature Publishing Group, <https://doi.org/10.1038/s41598-020-65862-9>. 640
641
642
643
62. Fock, V. Bemerkung zur Quantelung des harmonischen Oszillators im Magnetfeld. *Zeitschrift für Physik* **1928**, *47*, 446–448. <https://doi.org/10.1007/BF01390750>. 644
645
63. Govorov, A.O.; Ulloa, S.E.; Karrai, K.; Warburton, R.J. Polarized excitons in nanorings and the optical Aharonov-Bohm effect. *Physical Review B* **2002**, *66*, 081309. Publisher: American Physical Society, <https://doi.org/10.1103/PhysRevB.66.081309>. 646
647
648
64. Fischer, A.M.; Campo, V.L.; Portnoi, M.E.; Römer, R.A. Exciton Storage in a Nanoscale Aharonov-Bohm Ring with Electric Field Tuning. *Physical Review Letters* **2009**, *102*, 096405. Publisher: American Physical Society, <https://doi.org/10.1103/PhysRevLett.102.096405>. 649
650
651
65. Aharonov, Y.; Bohm, D. Significance of Electromagnetic Potentials in the Quantum Theory. *Physical Review* **1959**, *115*, 485–491. Publisher: American Physical Society, <https://doi.org/10.1103/PhysRev.115.485>. 652
653
654
66. Chaplik, A.V. Aharonov-Bohm effect for composite particles and collective excitations. *Journal of Experimental and Theoretical Physics Letters* **2002**, *75*, 292–296. <https://doi.org/10.1134/1.1481465>. 655
656
67. Ding, F.; Akopian, N.; Li, B.; Perinetti, U.; Govorov, A.; Peeters, F.M.; Bof Bufon, C.C.; Deneke, C.; Chen, Y.H.; Rastelli, A.; et al. Gate controlled Aharonov-Bohm-type oscillations from single neutral excitons in quantum rings. *Physical Review B* **2010**, *82*, 075309. Publisher: American Physical Society, <https://doi.org/10.1103/PhysRevB.82.075309>. 657
658
659
660
68. Li, B.; Peeters, F.M. Tunable optical Aharonov-Bohm effect in a semiconductor quantum ring. *Physical Review B* **2011**, *83*, 115448. Publisher: American Physical Society, <https://doi.org/10.1103/PhysRevB.83.115448>. 661
662
663